Channel Characterization and Modeling for Optical Wireless Body-Area Networks

Oussama Haddad, Mohammad-Ali Khalighi, Stanislav Zvanovec, Mouloud Adel

Received 22 April 2020; revised 26 May 2020; accepted 27 May 2020. Date of publication 1 June 2020; date of current version 18 June 2020.

Digital Object Identifier 10.1109/OJCOMS.2020.2999104

Channel Characterization and Modeling for Optical Wireless Body-Area Networks

OUSSAMA HADDAD[1], MOHAMMAD-ALI KHALIGHI[1] (Senior Member, IEEE), STANISLAV ZVANOVEC[2] (Senior Member, IEEE), AND MOULOUD ADEL[1]

[1]Aix-Marseille University, CNRS, Centrale Marseille, Institut Fresnel, Marseille, France

[2]Department of Electromagnetic Field, Faculty of Electrical Engineering, Czech Technical University in Prague, 16636 Prague, Czech Republic

CORRESPONDING AUTHOR: M.-A. KHALIGHI (e-mail: ali.khalighi@fresnel.fr)

This work was supported by the European Union's Horizon 2020 Research and Innovation Programme under the Marie Skłodowska-Curie Grant Agreement 764461 (VisIoN).

ABSTRACT We address channel characterization and modeling for medical wireless body-area networks (WBANs) based on the optical wireless technology. We focus on the intra-WBAN communication links, i.e., between a set of medical sensors and a coordination node, placed on the patient's body. We consider a realistic mobility model, e.g., inside a hospital room, which takes into account the effect of shadowing due to body parts movements and the variations of the underlying channels. To take into account the global and local user mobility, we consider a dynamic model based on a three-dimensional animation of a walk cycle, as well as walk trajectories based on an improved random way-point mobility model. Then, Monte Carlo ray-tracing simulations are performed to obtain the channel impulse responses for different link configurations at different instants of the walk scenarios. We then derive first- and second-order statistics of the channel parameters such as the channel DC gain, delay spread, and coherence time, and furthermore, propose best fit statistical models to describe the distribution of these parameters for a general scenario.

INDEX TERMS Wireless body-area networks, optical wireless communications, channel modeling, channel characterization, ray tracing, user mobility.

I. INTRODUCTION

THE GLOBAL increase in life expectancy and the increase of chronic and cardiovascular diseases have resulted in a growing interest in developing medical telemonitoring and telecare systems [1]–[4]. These systems can be realized through the use of medical on-body sensor networks, also known as wireless body-area networks (WBANs). They consist of networks of medical sensors located inside, on, or outside the human body. The sensors are connected to a central coordinator node (CN), located on the body, which collects the incoming data and typically forwards them to an access point (AP). This latter, in turn, performs preprocessing on this data before transmitting them, e.g., to a medical center, where they are stored and analyzed by the medical staff.

Medical WBANs have specific requirements that differentiate them from other networks, including high reliability, low energy consumption, and high data security [5]–[7]. When based on the radio-frequency (RF) technology, they should also ensure a low specific absorption rate (SAR) level, as considered in the IEEE 802.15.6 standard [5], [8]. Since most currently-proposed WBAN solutions use RF waves in the unlicensed industrial, scientific, and medical (ISM) frequency band, there is a high risk of electromagnetic interference with the other existing networks. Moreover, RF links are in general more subject to channel time variations due mainly to small-scale fading [9], [10]. These considerations have motivated the investigation of alternative (or complementary) technologies such as optical wireless communications (OWC) for medical WBANs [7]. Here, the main advantages of OWC include their immunity to external interference, not being affected by small-scale (multi-path) fading, as well as their inherent security due to the confinement of light in indoor spaces [6].

A. CHANNEL CHARACTERIZATION AND MODELING, STATE OF THE ART

Obviously, accurate characterization and modeling of the optical channel is a prerequisite to the design of efficient transmission techniques ensuring the requirements of medical WBAN systems. Extensive work has been done so far on wireless optical channel modeling and several methods have been proposed to calculate the optical channel impulse response (CIR) mainly for the case of a static indoor channel [11], [12]. The pioneering works were these of [13]–[15], which are based on a time-domain ray-tracing approach. Some other works such as [16]–[18] used a Monte Carlo ray-tracing (MCRT) based approach with the advantage of faster computation. Reduced computational time can also be achieved by switching to the frequency domain by estimating the channel transfer function [19]. The accuracy of these algorithms was verified experimentally using infrared (IR) sources, e.g., in [20], [21].

An important point is to model time-varying channels, whose their dynamics can be taken into account by adding a mobility model to the previous methods. For instance, a statistical modeling approach was proposed in [22], [23], based on a large set of CIRs generated through simulations. Meanwhile, it was shown that the line-of-sight (LOS) channel gain follows a modified Gamma distribution, whereas the channel gain including LOS and diffuse components follows a modified Rayleigh distribution [23]. In [24], the effect of shadowing on a visible-light communication (VLC) system using multiple LEDs was investigated. An algorithm accounting for the human body shadowing effect was also proposed in [25]. Also, [26] investigated via simulations and experimentally an indoor VLC channel considering random movements of people, concluding a Rayleigh distribution for the channel gain. A distance-dependent VLC path loss model was presented in [27] for a user moving along different trajectories in a furnished indoor environment. Lastly, [28] studied the influence of random device orientations on the statistics of the received signal-to-noise (SNR) for a mobile user.

A few studies have considered channel characterization for optical WBANs in the IR band such as the work in [29], which was based on MCRT simulations using a dedicated software, called RapSor [30]. On the other hand, channel characterization for extra-WBAN links (i.e., between a CN and an AP located in the room) was considered in [31]–[34], where user mobility was considered based on uniformly distributed random user positions and orientations of the sources/detectors. The patient's body was modeled by a simple rectangular surface in [31], [33], and by a combination of three rectangular volumes in [34], whereas a static three-dimensional (3D) model was used in [32]. Recently, in [35], we considered extra-WBAN channel characterization and modeling using a similar MCRT approach as in the present work.

Notice that channel modeling for RF-based WBANs is a rather well-explored topic. For instance, in [36]–[38], an avatar derived from an animation software was used to characterize the intra-WBAN channels for different scenarios including walking, running, and getting up from a chair. A similar approach was adopted in [39] to study a dynamic soldier-to-soldier communication scenario. Another approach considered a mobility model based on motion capture (MoCap) data to study the extra-WBAN channel [40], [41]. Analytical models were also proposed to describe body postures and movements, as well as node mobility patterns, such as in [42], [43].

B. MOTIVATIONS AND MAIN CONTRIBUTIONS

In this work, we focus on channel characterization and modeling of intra-WBAN optical links. For the sake of user convenience, we exclude the use of the VLC technology and consider IR links between sensors and the CN. The main issue here resides in the mobility that requires accurate modeling by taking into account an acceptable level of body details and local mobility of body parts, in contrast to the previously-proposed simplified models presented in Section I-A. This accuracy is required since the movements of the body parts change the link geometry (related to body posture) between the transmitter (Tx) and the receiver (Rx), which could occasionally result in or LOS blockage or beam shadowing. Moreover, body movement inside a room exhibits a correlation between consecutive sequences of the walk trajectory, which needs to be taken into consideration for a realistic channel model. As a result, appropriate non-uniform mobility modeling needs to be considered within this context.

To the best of the authors' knowledge, there is no reported work on optical WBAN channel modeling that considers the effects of mobility and shadowing due to the body parts as well as a realistic body movement inside an indoor environment, which is the main contribution of this paper. We propose a dynamic model based on a 3D animation of the walk cycle to model body parts movement. We also introduce a modified random waypoint (RWP) mobility model to generate a realistic random trajectory of a patient inside a room, similar to some recent works in the RF domain [36]–[38], [41], [42]. Regarding the optical WBAN system, we consider a star network topology where 10 sensors located on different positions on the patient's body are connected to a CN. We study two possible locations for this latter, i.e., on the shoulder or the hip of the user as suggested by [29], [34]. We adopt the MCRT method to obtain the CIRs for the given configurations and at different instants of the walk scenario. We then derive first-order and second-order statistics for channel parameters such as the channel DC gain, delay spread, and coherence time. Based on these results, we provide a best-fit model to describe the statistical distributions of these parameters.

The particularity of our study is to provide valuable insight into the special characteristics of the optical WBAN channels, given the fundamental differences with RF-based WBANs, for instance, concerning high sensitivity to body shadowing and the absence of small-scale fading.

C. PAPER ORGANIZATION, NOTATIONS, AND ACRONYMS

The remainder of the paper is organized as follows. After introducing the theoretical concepts behind CIR computation via the MCRT approach in Section II, we describe the adopted methodology for the simulations in Section III. Next, we present in Section IV the simulation results on the temporal evolution of the channel gain and delay spread, as well as on their statistical distribution for the underlying intra-WBAN links. Lastly, Section V concludes the paper.

Notations: Boldface uppercase and lowercase letters are used for matrices and vectors, respectively. Also, $\delta(\cdot)$ denotes the Dirac delta function, $(.)^{\mathrm{T}}$ stands for vector transpose, $\|\cdot\|$ denotes Euclidean norm, $(.)$ is the scalar vector product, and $\vec{\omega}$ denotes the direction of the geometric vector ω, and Ω represents the hemisphere around a reflection surface. Lastly, $\vec{\boldsymbol{\omega}}$ denotes array of geometric vector directions.

NOMENCLATURE

3D	Three Dimensional
ACF	Auto-Correlation Function
AIC	Akaike Information Criterion
AP	Access Point
BRDF	Bidirectional Reflectance Distribution Function
CAD	Computer-Aided Design
CIR	Channel Impulse Response
CN	Coordinator Node
ECG	Electrocardiogram
EEG	Electroencephalogram
FWHM	Full Width at Half Maximum
IR	Infrared
ISI	Inter Symbol Interference
ISM	Industrial Scientific and Medical
LED	Light Emitting Diode
LOS	Line-Of-Sight
MCRT	Monte Carlo Ray-Tracing
NLOS	Non-Line-Of-Sight
OOK	On Off Keying
OWC	Optical Wireless Communication
PDF	Probability Distribution Function
RF	Radio Frequency
RWP	Random WayPoint
Rx	Receiver
SN	Sensor Node
SNR	Signal-to-Noise Ratio
STL	Standard Tessellation Language
Tx	Transmitter
VLC	Visible Light Communication
WBAN	Wireless Body-Area Network.

II. MODELING OF DYNAMIC CHANNEL

This section presents the basic theoretical concepts behind our approach for dynamic optical channel modeling. These concern the potential equation and its relation to CIR, and the RWP mobility model. Although, as we will explain later, we use the Opticstudio software for channel characterization, it is quite useful to relate the theoretical concepts to the software parameters and outputs for a better understanding of the method used.

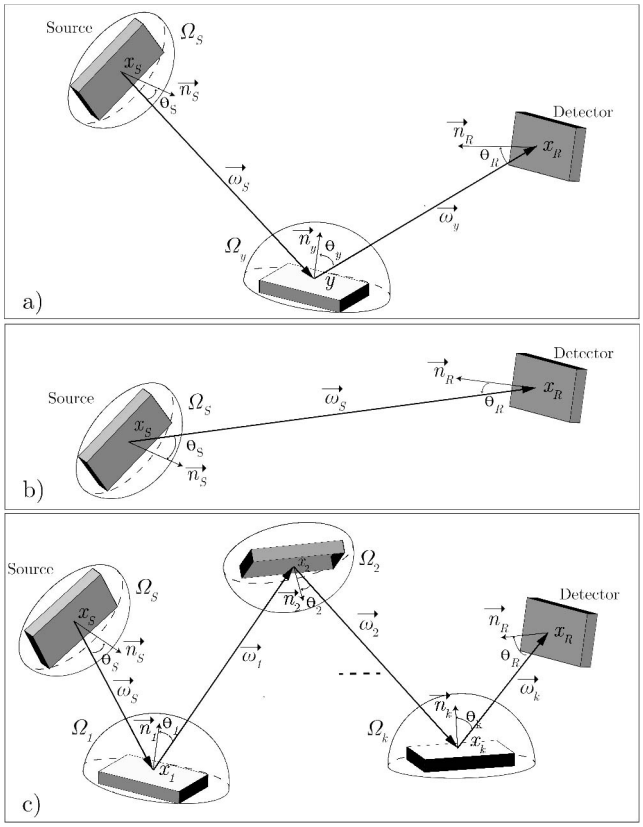

FIGURE 1. Illustration of potential function: a) single reflection case, b) LOS case, c) multiple reflection case.

A. POTENTIAL EQUATION

The potential equation is a recursive relation that expresses the potential of a surface to illuminate a virtual Rx. For a surface located at a given position x_S, its potential $W(x_S, \vec{\omega}_S)$ to illuminate a Rx at x_R along the direction $\vec{\omega}_S$ after reflection on a surface at position y (see Fig. 1(a)) is given by [44]:

$$W(x_S, \vec{\omega}_S) = g(x_S, \vec{\omega}_S) + \int_{\Omega_y} f_y(\vec{\omega}_y, \vec{\omega}_S) W(y, \vec{\omega}_y) \cos\theta_y \mathrm{d}\vec{\omega}_y, \tag{1}$$

where θ_y is the angle between the surface normal at y and the outgoing direction $\vec{\omega}_y$, and $g(x_S, \vec{\omega}_S)$ is a visibility function which equals 0 if the path from x_S to x_R is obstructed, and 1 otherwise. In fact, $g(x_S, \vec{\omega}_S)$ here indicates the LOS path, whereas the integral term describes the reflective paths. Also, $f_y(\vec{\omega}_y, \vec{\omega}_S)$ is the bi-directional reflection distribution function (BRDF) at point y. The total power P_e emitted by the source located at x_S can be written as:

$$P_e = \iint_{A_S \Omega_S} L_e(x_S, \vec{\omega}_S) \cos\theta_S \mathrm{d}\vec{\omega}_S \, \mathrm{d}A_S, \tag{2}$$

where A_S is the surface of the source and Ω_S is the upper half hemisphere centered around the point x_S. Also, $L_e(x_S, \vec{\omega}_S)$ is the radiance leaving x_S in the direction $\vec{\omega}_s$, expressed in W m^{-1} sr^{-1}, and θ_S is the angle between $\vec{\omega}_S$ and the surface normal to x_S, see Fig. 1(a). The corresponding received power P_r at x_R is related to the potential at x_S as follows [45]:

$$P_r = \iint_{A_S \Omega_S} L_e(x_S, \vec{\omega}_S) W(x_S, \vec{\omega}_S) \cos\theta_S \mathrm{d}\omega_S \mathrm{d}A_S. \tag{3}$$

For the LOS contribution, as illustrated in Fig. 1(b), the potential $W(x_S, \vec{\omega}_S)$ equals 1. We assume that the detector surface A_R and the source surface A_S are negligible compared to the distance d between x_S and x_R. Also, denoting by θ_R the angle between $\vec{\omega}_S$ and the normal vector of the detector $\vec{n}_R$, we have $\mathrm{d}\omega_S \approx \cos\theta_R A_R / d^2$. Then, from (3), the received power from the LOS is (see Fig. 1(b)):

$$P_r^{(0)} = R_e(\vec{\omega}_S) \frac{\cos\theta_S \cos\theta_R}{d^2} A_R, \tag{4}$$

where the superscript $.^{(0)}$ stands for the zero-reflection path, i.e., the LOS. Also, $R_e(\vec{\omega}_S)$ is the radiant intensity of the source expressed in W sr^{-1}. For a contribution that undergoes k reflections before arriving at the Rx, see Fig. 1(c), the corresponding received power $P_r^{(k)}$ can be written using (1) and (3) in recursive form as follows:

$$P_r^{(k)} = \iint_{A_S \Omega_S} \int_{\Omega_1} \cdots \int_{\Omega_k} G_k(\boldsymbol{x}, \vec{\boldsymbol{\omega}}) \mathrm{d}\omega_k \ldots \mathrm{d}\omega_1 \mathrm{d}\omega_S \mathrm{d}A_S, \tag{5}$$

where Ω_j denotes the hemisphere around the reflection surface x_j. Also,

$$G_k(\boldsymbol{x}, \vec{\boldsymbol{\omega}}) = L_e(x_S, \vec{\omega}_S) \cos\theta_S A_R \frac{\cos(\theta_R)}{d_k^2} \times \prod_{j=1}^{k} f_{x_j}(\vec{\omega}_{j-1}, \vec{\omega}_j) \cos\theta_{x_j}, \tag{6}$$

where $\boldsymbol{x}$ and $\vec{\boldsymbol{\omega}}$ denote the sets of the intersection points $x_S, x_1, \ldots, x_k$ and directions $\vec{\omega}_S, \vec{\omega}_1, \ldots, \vec{\omega}_k$, respectively. Here, d_k is the distance between the Rx and the last intersection point x_k, and $f_{x_j}(\vec{\omega}_{j-1}, \vec{\omega}_j)$ is the BRDF at x_j.

Equation (5) can be solved by deterministic [13] or non-deterministic approaches such as Monte Carlo integration methods [17]. Denoting the estimated received power by $\hat{P}_r$, the basic Monte Carlo method for solving (5) consists of taking N_{rays} samples from the hemisphere around x_S and taking the average. For a given sample i, we denote by $\boldsymbol{x}_i$ and $\vec{\boldsymbol{\omega}}_i$ the sets of intersection points $x_{iS}, x_{i1}, \ldots, x_{ik}$ and directions $\vec{\omega}_{iS}, \vec{\omega}_{i1}, \ldots, \vec{\omega}_{ik}$, with the occurrence probability $p(\boldsymbol{x}_i, \vec{\boldsymbol{\omega}}_i) = \prod_{j=1}^{k} p(x_{ij}, \vec{\omega}_{ij})$. We have:

$$\hat{P}_r = \frac{1}{N_{\text{rays}}} \sum_{i=1}^{N_{\text{rays}}} \frac{G_k(\boldsymbol{x}_i, \vec{\boldsymbol{\omega}}_i)}{p(\boldsymbol{x}_i, \vec{\boldsymbol{\omega}}_i)}, \tag{7}$$

where the term in the summation corresponds to the power of the i^{th} sample, that we denote by $P_{r,i}$.

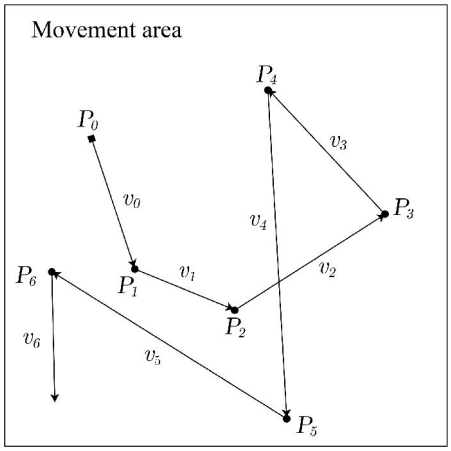

FIGURE 2. Illustration of the RWP mobility model for a node initially located at P_0.

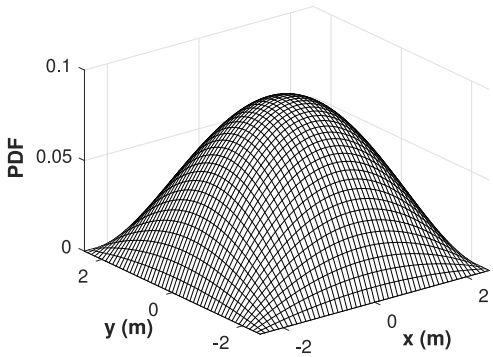

FIGURE 3. Spatial node distribution according to RWP in a rectangular area of size (5 m ×5 m).

B. RWP MOBILITY MODEL

By the RWP model, a mobile node chooses a random destination point P_m within the movement area $\mathcal{A}$ according to a uniform distribution, and moves toward it with a constant speed v_m (chosen randomly from an interval $[v_{\min}, v_{\max}]$), see Fig. 2. After reaching P_m, it stops for a random pause time before choosing a new destination point P_{m+1} and moves toward it with a new speed v_{m+1}. These steps are repeated until the simulation time is reached. For instance, an n-step walking process can be described by the couplets $\{(P_0, v_0), (P_1, v_1), \ldots, (P_n, v_n)\}$. Note that, for simplicity, in this work, we do not consider any pause time for the mobile node.[1] This way, the RWP model becomes similar to the random walk model. Denoting by x and y the Cartesian coordinates of a given position, the spatial distribution $f_{XY}(x, y)$ of positions in a rectangular area of size $a \times a$ can be approximated by [46]:

$$f_{XY}(x, y) \approx \frac{36}{a^6} \left(x^2 - \frac{a^2}{4}\right)\left(y^2 - \frac{a^2}{4}\right). \tag{8}$$

This distribution for the case of a rectangular room of dimension (5 m ×5 m) is shown in Fig. 3. We note that the positions

1. The reason is to simplify the "synchronization" of the local and global mobility models, as will be described later in Section III-D.

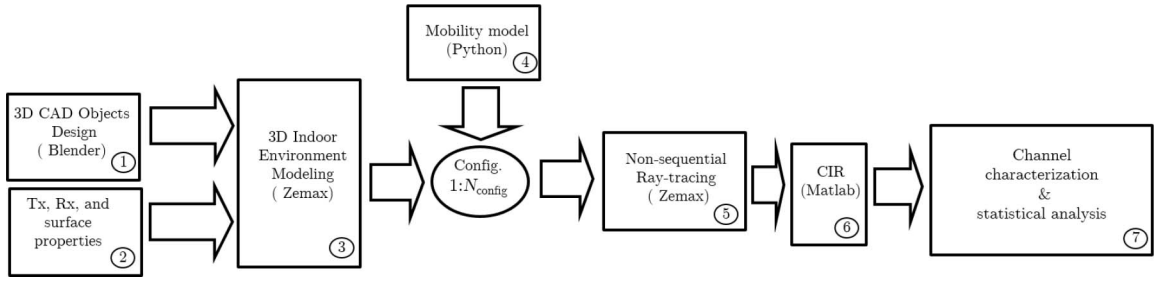

FIGURE 4. Adopted simulation methodology.

near to the room center have a higher probability than those at the corners, which is rather realistic for the movement of a person inside a room.

C. CHANNEL CHARACTERIZATION

In this work, we use the non-sequential ray-tracing feature of Opticstudio from Zemax [47], which is a licensed optical design software for MCRT simulations. The advantage of Opticstudio is its ability to model complex 3D environments. The ray-tracing output consists of a detailed database file of the generated rays, including their power and optical path length after each reflection. The CIR, $h(t)$, can then be estimated as follows.

$$h(t) = \frac{1}{N_{\text{rays}}} \sum_{i=1}^{N_{\text{rays}}} P_{r,i} \delta\left(t - \frac{d_i}{c}\right), \tag{9}$$

where c is the speed of light and d_i is the total distance that the i^{th} ray has traveled before reaching the detector. We use several metrics to analyze the obtained simulation results, including the channel DC gain and delay spread. The DC gain H_0 is defined as [48]:

$$H_0 = \int h(t)\mathrm{d}t. \tag{10}$$

Also, the root mean squared (RMS) delay spread τ_0 of the channel is defined by [6]:

$$\tau_0 = \sqrt{\frac{\int_0^\infty (t-\tau)^2 h^2(t)\mathrm{d}t}{\int_0^\infty h^2(t)\mathrm{d}t}}, \tag{11}$$

where τ is mean excess delay, given by:

$$\tau = \frac{\int_0^\infty t h^2(t)\mathrm{d}t}{\int_0^\infty h^2(t)\mathrm{d}t}. \tag{12}$$

For the case of dynamic WBAN channels, we will consider their statistical modeling by fitting the histogram of the channel gains to a given probability density function (PDF) such as Rayleigh, lognormal, Weibull, Nakagami, etc. To find the best fit model, we use the Akaike information criterion (AIC), defined as [49]:

$$\text{AIC} = -\log\left(L\left(\hat{\boldsymbol{\Theta}}|\boldsymbol{x}\right)\right) + 2p + \frac{2p(p+1)}{(N_{\text{p}} - p - 1)}, \tag{13}$$

where $\log(L(\hat{\boldsymbol{\Theta}}|\boldsymbol{x}))$ is the log-likelihood of the estimated model parameters $\boldsymbol{\Theta}$ of size p, conditioned on the data samples $\boldsymbol{x}$ of size N_{p}. The model corresponding to the minimum AIC value provides the best fit to the data.

To characterize channel time variations, we also consider the channel coherence time that is approximated by the time for which the autocorrelation function (ACF) falls below a certain value, e.g., 0.5 [6].

III. NUMERICAL SIMULATION OF INTRA-WBAN LINKS

A. SIMULATION METHODOLOGY

The block diagram of our simulation methodology is given in Fig. 4. The first step consists in building the 3D scene inside the Opticstudio simulator. The 3D objects are either created from built-in objects or imported using a 3D computer-aided design (CAD) software such as Blender [50] (Block ① in Fig. 4). We then define the reflective properties of these objects (e.g., the BRDF of the different surfaces), as well as the properties of the sources and detectors, i.e., Tx radiation pattern, detectors field-of-view (FOV), detector area, etc. (Block ②). By adding up these 3D objects, we construct the environment and its constituent reflectors (Block ③). The next step is to include the mobility model (Block ④). We use a Python script to load a set of N_{config} configurations describing objects' movements and orientations during the consecutive snapshots of a mobility scenario. Once the configuration is loaded, the script runs the non-sequential ray-tracing tool from Opticstudio (Block ⑤) that will be used to estimate the CIR for the given configuration, as explained in Section II-A. Afterward, based on the calculated CIRs, e.g., using MATLAB (Block ⑥), we analyze different channel metrics and their statistics (Block ⑦).

B. SENSOR PLACEMENT

We consider a set of 10 sensors nodes (SNs) on the patient's body, as shown in Fig. 5(a). The sensor positions correspond to the most likely placements for potential applications such as electroencephalogram (EEG: SN1 and SN2), electrocardiogram (ECG: SN3, SN4, and SN6), insulin pump (SN8), etc. To study the effect of CN placement, we consider two potential positions as suggested in [29], [34], i.e., on the shoulder and the hip, denoted by CN1 and CN2, respectively. Considering these two different CN locations provides

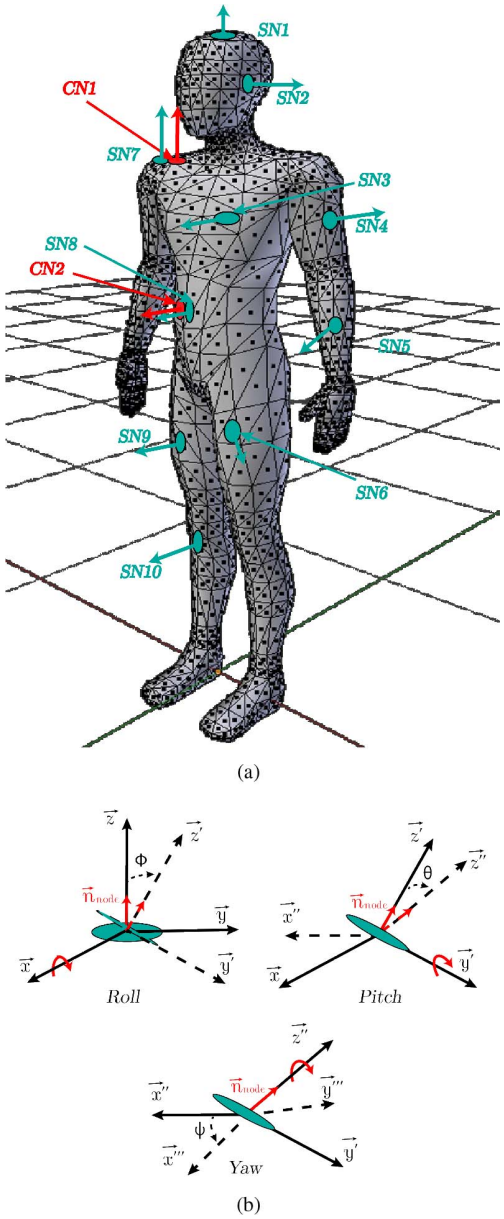

FIGURE 5. Illustration of the STL model of the body; (a) considered placements of SNs and CNs with the corresponding $\vec{n}_{\text{node}}$ vectors; (b) *xyz* intrinsic rotations made to direct the node along the orientation $\vec{n}_{\text{face}}$ of the triangular face: the Cartesian coordinates after roll-pitch-yaw rotations (in order) are denoted by $xy'z'$ (after roll rotation), $x''y'z''$ (after pitch rotation), and $x'''y'''z''$ (after yaw rotation).

sufficient insight on the channel statistics for different potential SNs. Note that, the selected location for the CN impacts the reliability of the links between the CN and SNs for the intra-WBAN links, as well as that of the link between the CN and the AP for the extra-WBAN link (given that the AP is likely placed on the room ceiling or wall). For CN1, the links are less sensitive to shadowing from body parts than for CN2, where they can be impacted by the arms of the user. Also, since CN2 is around the center of the network, there is less difference in its distance to the SNs, compared to CN1.

We model the human body by a 3D STL (Standard Tessellation Language) mesh object [51], which is a widely used file format in CAD tools to describe surfaces of a 3D object. It consists of a set of vertices, edges, and faces to define the shape of the object. Vertices are defined by their corresponding 3D coordinates and faces by the vertices that delimit them, as well as by their normal vector $\vec{n}_{\text{face}}$. We represent the patient's body by a set of 902 vertices, connected into 1800 triangular faces, as shown in Fig. 5(a), allowing sufficient precision for the simulations. We then place each SN on a triangular face, where its position and orientation are defined by the face center coordinates and its normal vector $\vec{n}_{\text{face}}$, respectively. To direct the node, initially oriented along $\vec{z}$, towards the face's normal vector $\vec{n}_{\text{face}} = (n_x, n_y, n_z)^T$, we apply the Davenport yaw-pitch-roll intrinsic chained rotation [52] to the reference vector $\vec{z} = (0, 0, 1)^T$, as illustrated in Fig. 5(b). The corresponding rotation matrix, taking into account roll, pitch, and yaw rotations around $\vec{x}$, $\vec{y}$, and $\vec{z}$, respectively, can be expressed as:

$$\begin{aligned}\boldsymbol{R} &= \boldsymbol{R}_x(\phi)\boldsymbol{R}_y(\theta)\boldsymbol{R}_z(0)\\ &= \begin{pmatrix} \cos\theta & 0 & \sin\theta \\ \sin\phi\sin\theta & \cos\phi\cos\theta & -\sin\phi\cos\theta \\ -\cos\phi\sin\theta & \sin\phi & \cos\phi\cos\theta \end{pmatrix}. \quad (14)\end{aligned}$$

Here, ϕ and θ denote the roll and pitch angles, respectively. We have set the yaw angle to zero because such rotations are included in the rotations of the corresponding faces. In fact, as shown in Fig. 5, the orientations of the nodes, and hence the vectors $\vec{n}_{\text{node}}$ are changed following the body's position and local mobility. Therefore, the yaw angle, which is with respect to $\vec{n}_{\text{face}}$, is set to zero without having an impact on the orientation of the node, as its corresponding rotation only tilts the node around $\vec{z}$ in the xy plane of the face. The orientation of the node is hence obtained from $\vec{n}_{\text{node}} = \vec{n}_{\text{face}} = \boldsymbol{R}\vec{z}$ and (14):

$$\begin{aligned}\phi &= \text{atan2}\big(-n_y, n_z\big), \quad \text{with } \phi \in [-\pi, \pi],\\ \theta &= \arcsin n_x, \quad \text{with } \theta \in [-\pi/2, \pi/2], \quad (15)\end{aligned}$$

where atan2 stands for the two-argument arctangent [53].

Table 1 summarizes the SN and CN positions on the body and their corresponding rotation angles, as well as the Cartesian coordinates of the unit vector $\vec{n}_{\text{node}}$ (after rotation) for the *anatomical* position configuration (i.e., at rest position). The considered body height, width, and depth are $(1.7 \times 0.3 \times 0.2)$ m^3, which correspond to the typical body shape of an adult person.

C. USER MOBILITY MODELING

To account for user mobility, we should consider at the same time the local mobility, which concerns body parts movements, and the global mobility, which concerns the movements of the whole body inside the room. We describe the local mobility of the body by a 3D animation of a walk cycle created (manually) using the Blender software [50]. Guidlines for creating the animation can be found in [54]. The animation consists of a set of $N_{\text{f}} = 27$ frames, representing the body at different instants of the walk cycle,

TABLE 1. Sensor and coordinator node positions and orientations as considered in Fig. 5(a). The last column indicates the corresponding cartesian coordinates of the unit vectors $\vec{n}_{\text{node}}$ (after rotation).

Node	x (m)	y (m)	z (m)	$\phi(^\circ)$	$\theta(^\circ)$	$\vec{n}^T_{\text{node}}$
SN 1	0.01	−0.04	1.63	22.84	11.95	$(0.21, -0.38, 0.9)$
SN 2	0.07	−0.01	1.56	−4.88	84.74	$(1.0, 0.01, 0.09)$
SN 3	0.18	−0.04	1.24	82.73	44.32	$(0.7, -0.71, 0.09)$
SN 4	0.23	0.08	1.18	76.27	63.18	$(0.89, -0.44, 0.11)$
SN 5	0.26	0.05	0.95	80.68	33.94	$(0.56, -0.82, 0.13)$
SN 6	0.10	−0.08	0.74	89.45	11.96	$(0.21, -0.98, 0.01)$
SN 7	−0.18	−0.01	1.37	19.82	−5.91	$(-0.1, -0.34, 0.94)$
SN 8	−0.10	−0.04	1.05	87.60	−47.97	$(-0.74, -0.67, 0.03)$
SN 9	−0.10	−0.04	0.59	106.18	−25.55	$(-0.43, -0.87, -0.25)$
SN 10	−0.09	0.00	0.15	87.96	−22.89	$(-0.39, -0.92, 0.03)$
CN 1	−0.19	−0.02	1.36	24.37	−7.97	$(-0.14, , -0.41, 0.9)$
CN 2	−0.07	−0.07	1.02	87.63	−27.46	$(-0.46, -0.89, 0.04)$

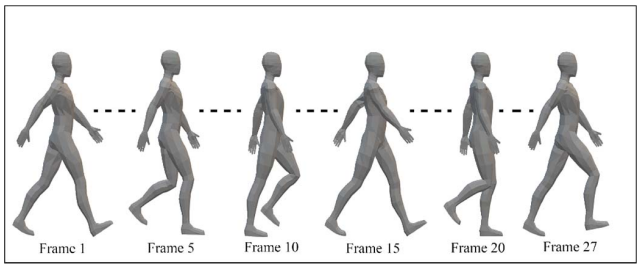

FIGURE 6. Illustration of the local mobility during a walk cycle.

as illustrated in Fig. 6.[2] Note that as the result of this body movement, the positions and orientations (i.e., angles ϕ and θ) of the SNs will change since the body configuration is different from one frame to another. To account for these changes, we use (15) to calculate the new SNs' positions and orientations in each frame (based on the position and orientation of the corresponding faces on the mesh object). This way, the set of five matrices $\boldsymbol{X}, \boldsymbol{Y}, \boldsymbol{Z}, \boldsymbol{\phi}$, and $\boldsymbol{\theta}$ of size $(N_{\text{f}} \times 12)$ will represent nodes movements along the walk cycle (10 SNs plus 2 CNs). The minimal and maximal ranges of variations of ϕ and θ for each sensor and coordinator node during local mobility are provided in Appendix A.

As concerns the global user mobility, as discussed in Section II-B, we use the RWP model to generate a random sequence of trajectory points $\{(P_{x_{\text{i}}}, P_{y_{\text{i}}}), (P_{x_{\text{i}+1}}, P_{y_{\text{i}+1}}), \vec{v}_{\text{i}}\}$, with i referring to a given time instance. We then calculate the appropriate time step Δt that synchronizes the local and global mobility models. By this approach, consecutive animation frames are changed each Δt, which is calculated based on the distance d_{cycle} traveled by the user during a walk cycle with a velocity v_{user}, as follows:

$$\Delta t = \frac{1}{N_{\text{f}}} \frac{d_{\text{cycle}}}{v_{\text{user}}}, \tag{16}$$

Referring to the general model in Section II-B, here, for the sake of simplicity, we consider a constant speed of $v_{\text{user}} = 0.45\,\text{m/s}$ for all user movements, which is a reasonable value. Also, considering a reasonable d_{cycle} of 2 m [55], [56], and setting $N_{\text{f}} = 27$, which has been verified to capture the movement pattern, we have $\Delta t \approx 0.17$ s. Note that with the classical RWP model, the user moves in a straight line from one point to another, producing a sharp rotation when reaching a waypoint. To consider a more realistic model, we propose here to improve the RWP model by moving the user along a curved path rather than straight lines. For this, we interpolate over the waypoints using a 3-order polynomial. Note that the spatial node distribution with this proposed approach is close to that with the classical RWP model, shown in Fig. 2, yet with slightly more spreading with respect to the center of the room. However, due to this 3-order polynomial interpolation, the actual user speed varies between 0.06 and 1.36 m/s, with the mean 0.38 m/s and the standard deviation 0.19 m/s. The higher speed values correspond to straight trajectories and the lower values are obtained near to rotation points. It is worth mentioning that this interpolation will also affect the degree of arms and legs swing. Nevertheless, for the sake of modeling simplicity, we do not modify the motion cycle accordingly, as this is a rather minor issue, given the relatively low speed (walk scenario) and relatively large coherence times (around a few seconds, as we will show later in Section IV-E). Overall, the interest of the proposed mobility model is the adequate description of realistic walk scenarios by favoring the positions in the vicinity of the room center and by taking into account a more smooth walk trajectory (avoiding sharp rotations). This especially concerns the statistics of channel time variations, where by avoiding unrealistic abrupt changes in the node direction, the estimated ACF and channel coherence time (see Section IV-E) are more realistic.

The resulting model can be described by the matrix $[\boldsymbol{p}_x, \boldsymbol{p}_y, \boldsymbol{\gamma}]$, where, for instance, $\boldsymbol{p_x}$ is the vector of x coordinates $P_{x_{\text{i}}}$ of the considered trajectory points, and $\boldsymbol{\gamma}$ is the vector of rotation angles γ_{i}, corresponding to the global rotation around $\vec{z}$ of the body, after the i$^{\text{th}}$ time instance:

$$\gamma_{\text{i}} = \arccos \frac{\vec{v}_{\text{i}} \cdot \vec{n}_{\text{body}}}{\|\vec{v}_{\text{i}}\| \, \|\vec{n}_{\text{body}}\|}, \tag{17}$$

where $\vec{v}_{\text{i}}$ is the corresponding instantaneous velocity and $\vec{n}_{\text{body}} = -\vec{y}$ is the initial vector normal to the body.

2. Note that here we consider the case of "normal" walking, which is reasonable for the case of medical surveillance of patients or elderly people, considered in this work. For studying specific walk scenarios with more precision, a more detailed model based on motion capture could be used.

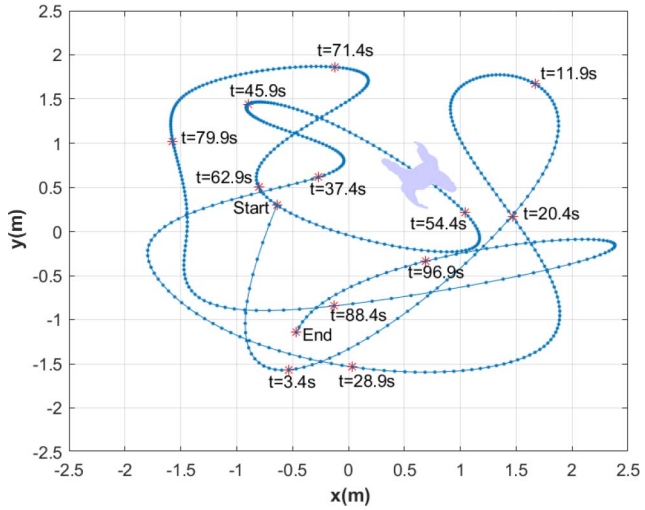

FIGURE 7. Top view of the typical user trajectory generated with the proposed improved RWP model for $N_p = 588$ positions.

Figure 7 illustrates the top view of a typical trajectory inside the room, generated using our proposed method. We can see that the generated trajectory is smooth and more realistic than the classical RWP (compare with Fig. 2).

D. ENVIRONMENT DESCRIPTION AND PARAMETERS SPECIFICATION

We consider at each SN an IR LED at $\lambda_0 = 850$ nm wavelength with full width at half maximum (FWHM) of $\Delta\lambda = 30$ nm, modeled by the typical Lambertian radiation of order $m = 1$. For CNs, we consider a photo-detector of 1 cm^2 active area (considered as typical value in the related literature) without any lens, and the Rx FOV is assumed to be 60°. Since in this work we are interested in the effects of body shadowing and user mobility on the channel metrics, we consider the case of an empty room as illustrated in Fig. 8 of dimension $(5 \times 5 \times 3)$ m^3, with plaster walls and ceiling, and pinewood floor. The classical Lambertian BRDF is used for the materials [11] while taking into account the wavelength dependency of their reflectivity as in [18], [57]. The body itself is assumed to be absorbent, given the low reflectivity of skin, compared to that of the walls [58]. Note that by assuming an absorbing body, we are considering the worst-case scenario where we have the maximum effect of beam shadowing. At least 3-order reflections are considered for beam propagation. Note that, although the room dimension can affect channel characteristics such as the DC gain and the delay spread, it has a negligible effect on their overall trend [23]. Also, given the typically low data-rates that are used in medical WBANs, the room furniture has a negligible impact on the main characteristics of the channel [31], [59]. At each user position, and from each SN, $N_{\text{rays}} = 2.5 \times 10^7$ rays are used for MCRT simulations with Opticstudio, insuring sufficient accuracy in the obtained CIRs. Table 2 summarizes the main parameters we use in our simulations.

TABLE 2. Simulation parameters.

Tx (SN)	m	1
	λ_0	850 nm
	$\Delta\lambda$	30 nm
Rx (CN)	FOV	60°
	Area	1 cm^2
Room	Dimensions	$(5 \times 5 \times 3)$ m^3
	Wall Reflectivity	0.83 (Plaster)
	Floor Reflectivity	0.87 (Pinewood)
	Ceiling Reflectivity	0.83 (Plaster)
Body	Dimensions	$(1.7 \times 0.3 \times 0.2)$ m^3
	Reflectivity	absorbing

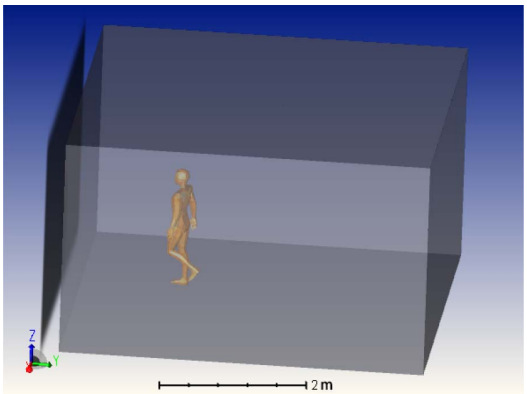

FIGURE 8. A snapshot of the simulated random walk inside an empty room with Opticstudio.

IV. NUMERICAL RESULTS

We provide here a set of simulation results to characterize the intra-WBAN IR optical channel. We consider three different cases of standing, local mobility, and global mobility configurations:

- In the standing configuration, the body is in anatomical position at the center of the room, which is the worst case for NLOS links as the distance from the reflectors is maximal. We have $N_{\text{config}} = 1$.
- For the local mobility configuration, the body has a fixed position at the center of the room but moves its parts (i.e., arms, legs, etc.) following the walk cycle described in Section III-C. Indeed, the interest in considering the local mobility case is to gain insight into the effects of body parts movement. For this case, we have $N_{\text{config}} = N_{\text{f}} = 27$.
- The global mobility case involves both the movements of the body inside the room (according to the proposed modified RWP model) and the local mobility of the body parts. Considering a simulation time of 100 sec, the total number of samples for the particular trajectory in Fig. 7 is $N_{\text{p}} = 588$. We have $N_{\text{config}} = N_{\text{p}}$.

The analysis of the obtained simulation data is presented in the following subsections.

A. CHANNEL DC GAIN

First, to study the channel attenuation, we analyze the average channel gain $\bar{H}_0$ and its standard deviation σ_0 for each

TABLE 3. Mean H_0(in dB) and standard variation σ_0 of the channel gain for different intra-WBAN links corresponding to CN1, for the three considered configurations.

SN	Standing	Local mobility		Global mobility	
	H_0	$\bar{H}_0$	σ_0	$\bar{H}_0$	σ_0
1	−53.45	−53.41	0.15	−52.36	0.67
2	−57.52	−57.76	0.15	−56.38	0.8
3	−56.27	−56.44	0.26	−55.3	0.81
4	−57.17	−57.83	0.35	−56.68	0.68
5	−56.32	−56.87	0.72	−55.96	0.9
6	−56.05	−56.76	0.86	−55.8	1.06
7	−53.57	−53.34	0.38	−52.01	1.36
8	−55.63	−56.27	0.66	−55.26	1.35
9	−56.22	−56.17	0.75	−55.58	1.08
10	−56.24	−56.81	0.56	−56.37	0.59

TABLE 4. Mean H_0(in dB) and standard variation σ_0 of the channel gain for different intra-WBAN links corresponding to CN2, for the three considered configurations.

SN	Standing	Local mobility		Global mobility	
	H_0	$\bar{H}_0$	σ_0	$\bar{H}_0$	σ_0
1	−55.79	−55.98	0.26	−55.17	0.65
2	−58.21	−57.38	0.52	−56.27	1.06
3	−55.7	−54.76	0.45	−53.48	1.41
4	−57.02	−56.54	1.06	−55.44	1.59
5	−55.51	−55.19	0.76	−54.01	1.52
6	−54.05	−53.43	1.11	−52.24	1.5
7	−55.6	−56.77	0.21	−55.81	0.75
8	−53.72	−53.81	0.46	−52.28	1.83
9	−52.98	−53.28	0.36	−51.88	1.56
10	−53.47	−54.03	0.97	−52.86	1.58

intra-WBAN link in the three above mentioned configurations. These results are presented in Tables 3 and 4 for the cases of CN1 and CN2, respectively.

1) STANDING CONFIGURATION

Obviously, for this configuration, we have $\bar{H}_0 = H_0$ and $\sigma_0 = 0$. We can see that those SNs which have the same orientation as the CN (e.g., SN7 for CN1, and SN9 for CN2) have a higher $\bar{H}_0$ (around −53 dB) compared to the other sensors. This can be explained by the presence of a strong first-order reflection contribution and would suggest, when it is possible, directing the nodes towards the same reflection surfaces, especially for sensors that do not move considerably. We can also see that SNs that are partially blocked by the body have a lower $\bar{H}_0$, which shows the impact of body shadowing on the channel gain. This is the case for most links to CN1; for instance, $\bar{H}_0 = -57.5$ and −57.1 dB for SN2 and SN4, respectively. We notice a higher $\bar{H}_0$ for SNs located on the lower part of the body for the case of CN2, with differences with respect to CN1 case on the order of 2 to 3 dB. For SN2 and SN4, we have similar results for CN1 and CN2, whereas for SN1 and SN7, $\bar{H}_0$ is about 2 dB higher for CN1. Lastly, note that the relatively low difference between the channel gains of different links can be justified by the relatively high reflectivity of walls in the case of IR transmission.

2) LOCAL MOBILITY CONFIGURATION

We observe similar behavior in $\bar{H}_0$ as in the previous case. For the case of CN2 (located on the right side of the hip) and compared to the standing configuration, we notice that, reasonably, $\bar{H}_0$ decreases for SNs located on the right side of the body, whereas it increases for SNs on the left side. For the case of CN1, we notice an increase in $\bar{H}_0$ for SN1 and SN7 and a decrease of it for the other SNs. Focusing on σ_0, we notice that it is, in general, higher for the case of CN2 compared to CN1: it ranges between 0.15 to 0.86 dB for the former case and between 0.21 to 1.11 dB for the latter case. For both CNs, the largest σ_0 values are observed for SNs placed on the legs and arms, while the lowest values are observed for SNs that are rather fixed during the local mobility (e.g., SN1 and SN7, placed on the head and the shoulder, respectively). An exception concerns SN8, which experiences periodic shadowing from the right arm, which makes its variations more important despite its relatively low mobility.

TABLE 5. Mean and standard deviation (in ns) of the RMS delay spread for different intra-WBAN links corresponding to CN1, for the three considered configurations.

SN	Standing	Local mobility		Global mobility	
	τ_0	$\bar{\tau}_0$	σ_τ	$\bar{\tau}_0$	σ_τ
1	4.34	3.81	0.32	3.85	0.63
2	12.20	12.61	0.28	12.46	2.02
3	9.25	10.07	0.18	10.08	2.30
4	9.31	9.84	1.32	11.27	1.37
5	8.57	9.17	0.95	10.02	1.58
6	7.23	8.33	0.45	9.19	1.63
7	4.15	3.95	0.97	4.06	0.95
8	6.89	7.16	0.14	8.69	2.51
9	6.13	6.78	0.41	8.62	1.94
10	6.53	6.40	0.25	8.27	1.65

3) GLOBAL MOBILITY CONFIGURATION

We observe a similar trend as in the previous case with a general increase in $\bar{H}_0$ for all links on the order of 1 dB. This was expected since with the body rotations and movements, for the positions that are close to the walls, we get a higher $\bar{H}_0$. Compared to the local mobility configuration, here σ_0 increases for all SN links due to more significant mobility, ranging in 0.59 to 1.36 dB for CN1 and 0.65 to 1.83 dB for CN2, while following a similar trend as observed for the local mobility case. This shows that body position and orientation inside the room have a large impact on the variations of H_0.

Comparing the cases of CN1 and CN2, as expected, a higher $\bar{H}_0$ is obtained for SNs located on the upper part of the body in the case of CN1, and vice versa. For instance, the difference between $\bar{H}_0$ for the cases of CN1 and CN2 is about 2.81 dB for SN1 and −3.5 dB for SN10. Concerning σ_0, we notice that in general using CN2 results in higher σ_0 compared to CN1. This can be explained by the fact that for the former case, the corresponding links experience more significant movements and frequent shadowing.

B. DELAY SPREAD

To evaluate the channel frequency selectivity, we have calculated the average delay spread $\bar{\tau}_0$ and its standard deviation

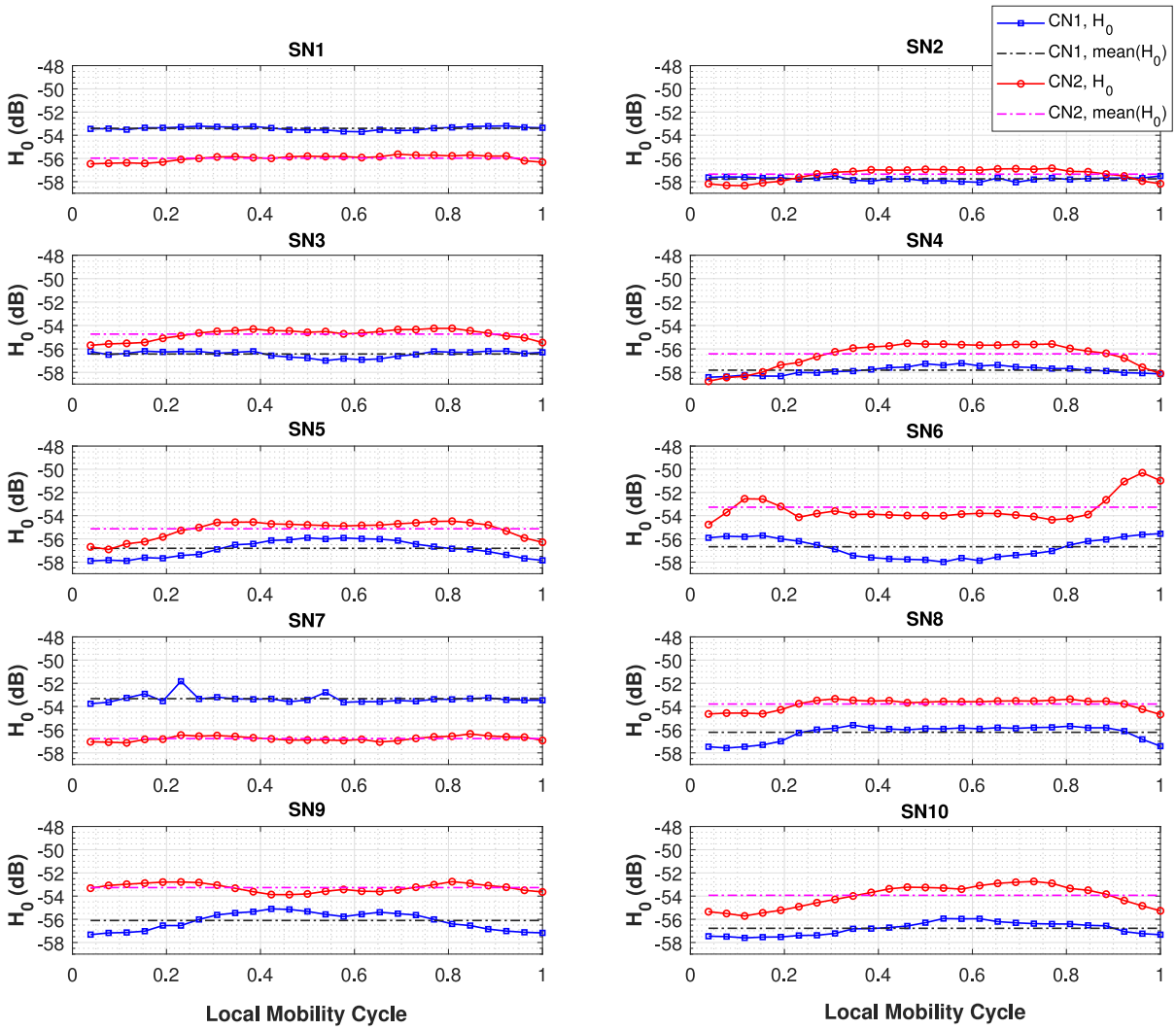

FIGURE 9. H_0 variations and its mean value (in dB) for the cases of CN1 and CN2 in the local mobility configuration.

TABLE 6. Mean and standard deviation (in ns) of the RMS delay spread for different intra-WBAN links corresponding to CN2, for the three considered configurations.

SN	Standing	Local mobility		Global mobility	
	τ_0	$\bar{\tau_0}$	σ_τ	$\bar{\tau_0}$	σ_τ
1	8.30	7.46	0.2	9.15	1.70
2	8.65	8.90	0.24	10.38	2.36
3	8.45	6.28	0.39	6.95	3.02
4	9.83	8.36	0.70	9.32	2.99
5	7.83	7.38	1.16	7.90	3.37
6	7.63	6.82	1.90	6.18	3.09
7	7.50	7.79	0.20	9.55	1.73
8	6.05	6.58	0.21	6.40	3.47
9	7.56	6.61	0.54	6.06	3.19
10	8.68	7.92	0.68	6.79	3.02

σ_τ for the three above-mentioned configurations. Results are presented in Tables 5 and 6 for the cases of CN1 and CN2, respectively.

For the standing configuration, $\bar{\tau_0} = \tau_0$ and $\sigma_\tau = 0$; with τ_0 ranging from 4 to 12 ns for the case of CN1 and from 6 to 10 ns for the case of CN2. We notice slight variations in $\bar{\tau_0}$ for the local and global mobility cases. It can decrease or increase depending on the corresponding position of the SN and the CN; for a given user position, the proximity to room walls could then result in a shorter or a longer path length. For the local mobility case, the changes in $\bar{\tau_0}$ with respect to the standing configuration are less than 1.1 ns for CN1 and less than 2.2 ns for CN2. These variations are less than 2.5 ns for the case of global mobility.

As concerns the delay spread standard deviation, for the cases of CN1 and CN2, respectively, σ_τ ranges in 0.1 to 1.3 ns and in 0.2 to 1.9 ns for the local mobility configuration, while it ranges in 0.6 to 2.5 ns and in 1.7 to 3.5 ns for the global mobility configuration. The reason for the increase in σ_τ for the global mobility case is that, compared to the local mobility case where the user is at the center of the room, here we experience more important variations of the link path length. For instance, for the positions close to the walls, links will have relatively shorter path lengths when the user is facing the wall, and inversely, they will have

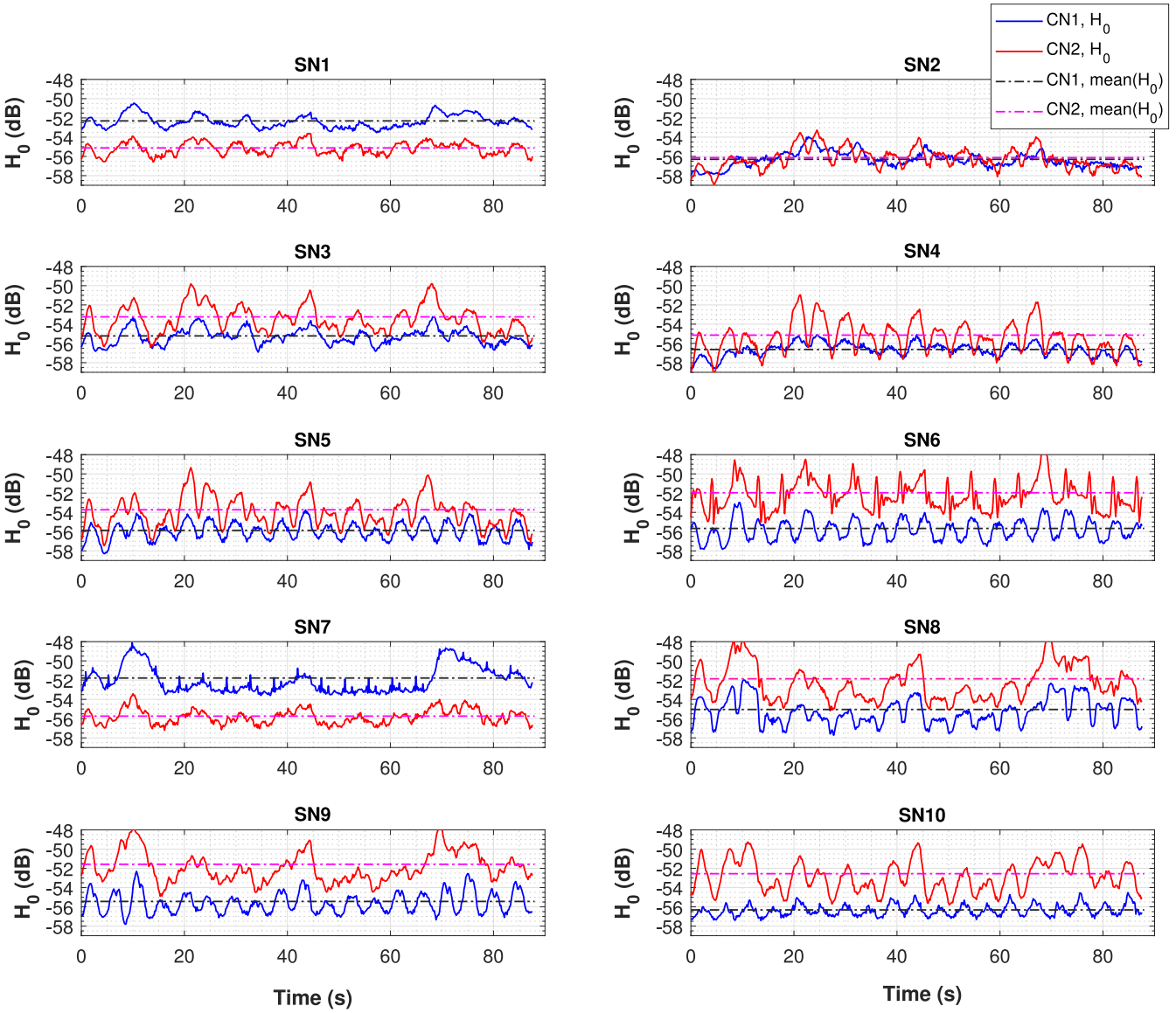

FIGURE 10. H_0 variations and its mean (in dB) for the cases of CN1 and CN2 over the global mobility trajectory.

longer path lengths when the back is against the wall. This results in more significant variations in τ_0, thus a larger σ_τ.

These results indicate that, when using a simple modulation technique such as on-off-keying (OOK), the communication channel can be considered as frequency non-selective roughly for data rates up to approximately 5 Mbps (considering a rather loose upper bound of 20 ns for τ_0), where no channel equalization is required at the Rx. Given that the data rates in typical intra-WBAN applications are less than 1 Mbps [5], [7], we can effectively neglect the channel delay dispersion in practice.

C. CHANNEL DYNAMIC BEHAVIOR

In order to evaluate the channel dynamics resulting from the user local and global mobility, let us investigate more closely the variations of the channel DC gain over time. This provides insight on the trend and the nature of the time variations of the channel DC gain (e.g., probable periodic patterns, stationarity properties, etc.) and its temporal correlation characteristics.

1) LOCAL MOBILITY

Figure 9 shows the time variations of H_0 for the cases of CN1 and CN2 in the local mobility configuration, where the abscissa represents the local mobility cycle, i.e., the frame number (see Fig. 6) normalized with respect to the total number of frames $N_{\text{frame}} = 27$. During the walk cycle, there is a periodic change of relative positions and orientations of the CNs and SNs. Also, link shadowing may occur resulting from body parts movement. For the body located at the center of the room and oriented toward one of the walls, these changes cause channel gain variations on the order of 0.2 to

2 dB for CN1, and 0.2 to 4 dB for CN2. This is consistent with the results presented in Section IV-A. A more detailed description of these results is provided in Appendix B.

An important point is to study the effects of Tx half-angle and room dimensions on H_0, which are not easily predictable. Indeed, for instance, a narrower Tx beam would imply more multipath reflections due to the increased LOS blockage probability whereas a wider beam could result in decreased LOS path gain and an effectively increased contribution of the multipath reflections. To investigate this, we have repeated the simulations by changing the Tx Lambertian order m from 1 to 45, and the room size from (5×5) to (10×10); results are not shown for the sake of brevity. Interestingly, we globally noticed the same trend as before with increasing m, with an increase in H_0 variations around 1 dB compared with $m = 1$; lower variations were noticed for the case of CN2 except for SN6. For this latter, LOS (present when the left leg is sufficiently raised) is mostly lost with a more directional beam. Also, when enlarging the room size, we again noticed the same global trend for all SNs, with a decrease in H_0 around 0.48 dB per $1\,\mathrm{m}^2$ increase in the room size. Thus, the important result is that changing m or room size does not affect the general trend of the variations of the channel parameters.

2) GLOBAL MOBILITY

Figure 10 shows the time variations of the DC channel gain for CN1 and CN2 during the global mobility scenario, where the abscissa represents the absolute time, in accordance with what is represented in Fig. 7. We can see that generally, global mobility implies channel gain variations by adding a random component, as compared to the periodic local mobility case. We can see that a straight walk towards a wall increases the channel gain, while rotations can increase or decrease it. This underlines the significant impact of user and body parts movement on the optical intra-WBAN channel. The presented results also show more significant variations of H_0 for the case of CN2. This can be explained by the fact that CN1 is mostly oriented toward the ceiling during the walk cycle, and consequently, it is less affected by the variations of body proximity to the walls due to rotations. Similar to the case of local mobility (see Section IV-A2), the link between SN8 and CN2 experience periodic obstructions as a result of the right arm swinging back and forth during the walk cycle.

D. STATISTICAL ANALYSIS OF CHANNEL GAIN

Here, we present a statistical analysis of the DC channel gain H_0 for different SNs and CNs with the aim of proposing statistical models for their variations for the case of global mobility. Such a best-fit statistical channel model is in particular useful for the theoretical performance evaluation and the link physical layer design without resorting to timely numerical simulations of the optical channel. For this purpose, based on the AIC metric, described in Section II-C, we have looked for the best fit of the corresponding

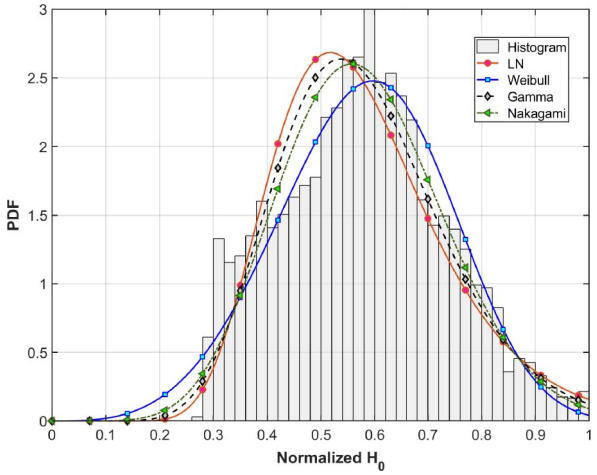

FIGURE 11. Illustration of best-fitting PDFs to the ensemble of H_0 related to CN1.

data obtained from the simulations to Gaussian, Lognormal (LN), Rician, Gamma, Nakagami, and Weibull distributions. Globally, the best fit was obtained for LN, Gamma, and Nakagami PDFs, recalled in the following.

- LN:

$$f_X(x) = \frac{1}{x\sigma\sqrt{2\pi}} \exp\left(\frac{-(\ln(x)-\mu)^2}{2\sigma^2}\right), \tag{18}$$

  where μ and σ stand for mean and standard deviation.
- Gamma:

$$f_X(x) = \frac{1}{b^a \Gamma(a)} x^{a-1} \exp\left(-\frac{x}{b}\right), \tag{19}$$

  where a and b are the shape and rate parameters, respectively, and $\Gamma(\cdot)$ is the gamma function.
- Nakagami:

$$f_X(x) = \frac{2\alpha^\alpha}{\Gamma(\alpha)\xi^\alpha} x^{2\alpha-1} \exp\left(-\frac{\alpha}{\xi} x^2\right), \tag{20}$$

  where α and ξ are the shape and scale parameters.

The corresponding fitted PDF parameters for each SN link together with the AIC values are presented in Appendix C, Tables 10 and 11, for the cases of CN1 and CN2, respectively.

Obviously, with this separate characterization of the different SN links, the estimated parameters highly depend on the exact locations and orientations of the sensors on the body. A more interesting approach is to find a global statistical model for the ensemble of the simulated H_0, i.e., corresponding to all links connecting a CN to different SNs. Compared to the SN-dependent distributions presented above, the obtained model will be simpler and more practical, i.e., with fewer parameters, but at the expense of less fitting accuracy. In fact, the SN-dependent model is useful for investigating special applications such as EEG and ECG recording, while the global model can be used as a generic channel model. Figures 11 and 12 illustrate the results of best-fit to different considered distributions, for the cases of

TABLE 7. Estimated parameters of best fit distributions to H_0 for the ensemble of simulated data.

CN	Best-fit PDFs	AIC	PDF parameters	
1	Nakagami	-4825	$\alpha = 3.72$	$\xi = 0.36$
	Gamma	-4772	$a = 13.79$	$b = 0.04$
2	Gamma	-3456	$a = 6.11$	$b = 0.07$
	LN	-3455	$\mu = -0.88$	$\sigma = 0.42$

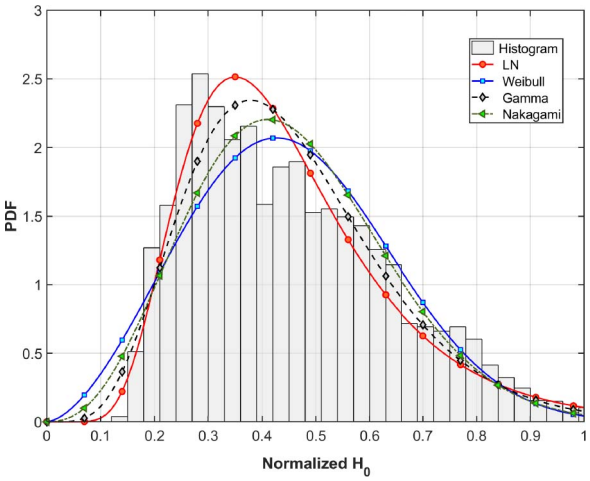

FIGURE 12. Illustration of best-fitting PDFs to the ensemble of H_0 related to CN2.

CN1 and CN2, respectively. The best-fit model, according to the AIC criterion, for the case of CN1 corresponds to the Nakagami distribution, whereas the Gamma distribution provides the best-fit for links related to CN2. Table 7 presents the corresponding parameters of the two best-fit distributions together with the AIC values. Like for the case of individual SN characterization, Gaussian, Weibull, and Rician distributions showed less tight fits. We suggest to use the Gamma distribution for both CN1 and CN2 cases since for the former, the difference between the corresponding Nakagami and Gamma PDFs in Fig. 11 is insignificant and AICs from Table 7 are rather close. Note that our results are consistent with the shadow fading models proposed for the case of RF-based WBANs, see for instance [8], [9].

E. CHANNEL COHERENCE TIME

Another important aspect in the design of appropriate signaling schemes concerns the statistical properties of the channel time variations. For this, we consider the ACF of the channel DC gain and coherence time for the different links. For instance, assuming a stationary channel, ACF indicates the correlation between different observation times, while the channel coherence time determines the packet length and the intervals of pilot transmission (used for channel estimation and probably for adaptive power control at the Tx) [9].

Figures 13 and 14 show the ACF of each SN link for the cases of CN1 and CN2, respectively, which are obtained based on the global mobility scenario. We notice an exponential decrease trend for all links, which is modulated by some oscillations whose frequency is related to the movements of the corresponding SN during the walk cycle. We notice such

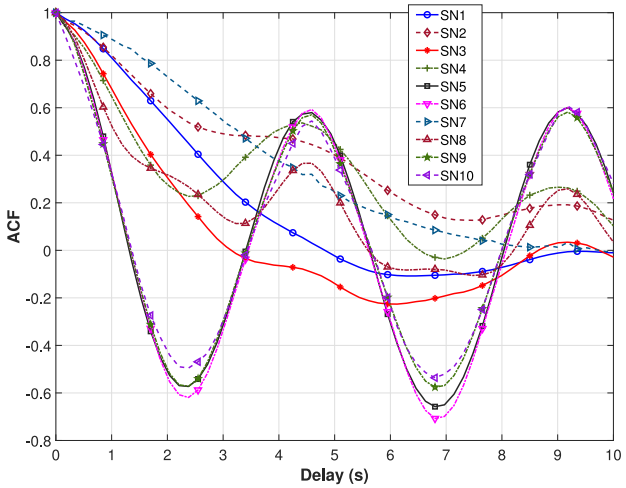

FIGURE 13. ACF for the links between different SNs and CN1.

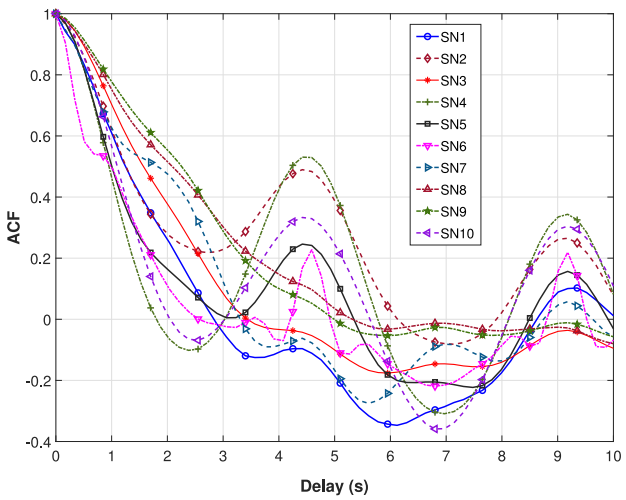

FIGURE 14. ACF for the links between different SNs and CN2.

TABLE 8. Channel coherence time: delays (in seconds) corresponding to 90 % and 50 % of the ACF.

SN	CN1		CN2	
	$T_{c,50}$	$T_{c,90}$	$T_{c,50}$	$T_{c,90}$
1	2.19	0.63	1.25	0.34
2	2.81	0.62	1.26	0.40
3	1.44	0.43	1.57	0.49
4	1.34	0.35	0.95	0.36
5	0.83	0.28	1.01	0.36
6	0.81	0.28	0.99	0.18
7	3.27	0.90	1.82	0.33
8	1.06	0.33	2.09	0.51
9	0.79	0.27	2.26	0.56
10	0.78	0.17	1.10	0.40

oscillations even for SNs that experience small body swing movements, i.e., SN3, SN8, however, with small amplitudes. Indeed, SN3 on the torso is less affected by body movements than those SNs on the legs or arms.

Based on these results, we have estimated the channel coherence time as the delay at which the ACF drops by 50 % and 90 %, that we will denote by $T_{c,50}$ and $T_{c,90}$, respectively.

The corresponding values are presented in Table 8. We notice a larger coherence time for SNs on the head and the torso, compared to those on the arms and the legs. For example, $T_{c,50}$ equals 1.01 and 2.09 sec for the links from SN5 and SN8 to CN2, respectively, which confirms a more stable channel for the latter link due to lower mobility.

Focusing on $T_{c,50}$, for instance, we note that it is on the order of hundreds of milliseconds to a few seconds, ranging between 0.78 to 3.27 sec for CN1 and between 0.95 to 2.26 sec for CN2. These relatively long coherence times indicate that optical intra-WBAN links have a slow time-varying nature, compared to their RF counterparts for which the coherence time is on the order of 0.025 to 0.07 sec [60], [61]. As a result, optical WBAN links benefit from larger packet sizes, a lower pilot overhead, and the possibility of using a simpler adaptive transmit power control over successive packets.

V. CONCLUSION

We investigated channel modeling and characterization for optical intra-WBANs links, i.e., between a set of SNs and a CN, during a walk scenario. The presented study provides useful insights into the effects of local and global user mobility and the corresponding beam shadowing. These effects were investigated using a realistic dynamic model based on a 3D animation of the walk cycle and a modified RWP mobility. MCRT-based simulations were then done using the Opticstudio software to obtain the CIRs for a set of SN and CN configurations at different instants of the walk scenario. The considered configurations cover the most likely locations of the CN and the SNs for a practical implementation of a medical WBAN. We presented comprehensive numerical results on the channel first- and second-order statistics, namely the DC gain, delay spread, ACF, and coherence time. The positions and orientations of SNs and CNs along with the body geometry were found to have a significant impact on the channel gain statistics. Nevertheless, overall, the channel can be considered as frequency non-selective for data-rates up to 5 Mbps when using the simple OOK signaling, for example. Consequently, ISI can be neglected for most medical WBAN applications.

For the case of local mobility with the body located at the center of the room and oriented toward one of the walls, we showed periodic changes of the channel gain with variations on the order of 0.2 to 4 dB. Changing the Tx beam divergence or the room size was found to affect negligibly the general trend of the channel parameters variations. On the other hand, global mobility was shown to cause a higher attenuation and more significant random variations of the channel gain, compared to the local mobility case. Based on the datasets obtained from simulations, we proposed best-fit models to describe the statistical distributions of the channel parameters, which are particularly helpful for studying the channel behavior (and consequently, the link performance) for physical or upper layer design. LN and Gamma distributions were found to provide the best AIC fit models for the channel attenuation.

Lastly, regarding channel time variations, optical intra-WBAN links were shown to have a slower time-varying nature (thus, of higher stability), as compared to their RF counterparts; the corresponding coherence times ranging between a few hundred milliseconds to a few seconds.

Note that the presented study was based on considering the typical body shape and dimensions of an adult person. The choice of body shape will determine the propagation of the rays in the vicinity of the human body. i.e., which rays will be absorbed by the body and which will be traced. The presented analysis, however, remains valid for the general case, in particular regarding the mobility effect. For example, for the case of a child, most propagation properties with respect to the local and global movements remain the same.

Future work will focus on the design of efficient signaling schemes for intra-WBAN links.

APPENDIX A
ANGLES RANGE OF VARIATION FOR EACH NODE

We provide here the minimal and maximal variations of ϕ and θ for each node, which are summarized in Table 9.

APPENDIX B
DETAILED DESCRIPTION OF CHANNEL TIME VARIATIONS FOR THE CASES OF LOCAL AND GLOBAL MOBILITY
A. LOCAL MOBILITY CASE

For the results presented in Fig. 9, the time variations of H_0 depend on the movement pattern of the body parts. We can explain these variations based on SNs locations as follows:

- *Sensors on the left arm:* For those sensors on the left arm (i.e., SN4 and SN5), H_0 experiences the same pattern for both CN1 and CN2 cases, where it varies by 2 dB when the left arm changes its orientation during the walk cycle. For the case of CN2, H_0 is also affected by the partial shadowing of the link by the right arm. The link from SN5 to CN2 experiences also a partial body shadowing when the left arm is behind the body.
- *Sensors on the head and the shoulder:* For SNs that move moderately such as SN1, SN2, and SN7, we logically observe only relatively small variations of about 0.7 dB due to the small changes of relative orientation angles. We also notice the same shadowing effects of the left arm for the link between SN2 and CN2, as before.
- *Sensors on the legs:* H_0 varies about 2 dB for the sensors on the legs (i.e., SN6, SN9, and SN10). For CN1, H_0 variations between SN6 on one hand, and SN9 and SN10, on the other hand, have opposite phases. For CN2, SN9 and SN10 have their highest H_0 when they have the same orientation. Also, due to the presence of a LOS between SN6 and CN2, H_0 increases considerably when the left thigh is raised to its maximum level.

TABLE 9. Ranges of variations of ϕ and θ for each sensor and coordinator node.

Node	$\phi(^\circ)$		$\theta(^\circ)$	
	min	max	min	max
SN1	22.83	22.84	11.95	11.95
SN2	-4.77	-3.03	84.77	85.17
SN3	73.79	77.89	33.39	38.45
SN4	57.05	103.72	60.16	77.83
SN5	47.23	121.15	33.53	48.41
SN6	46.19	114.3	11.23	40.33
SN7	10.77	11.11	-8.92	-4.33
SN8	95.56	97.58	-46.49	-21.59
SN9	65.64	130.59	-26.66	-22.93
SN10	71.15	150.27	-24.49	-23.96
CN1	11.63	17.96	-15.77	-4.72
CN2	93.74	96.30	-23.34	5.98

TABLE 10. Estimated parameters of best fit distributions to H_0 for the case of CN1; global mobility configuration.

SN	Best-fit PDFs	AIC	PDF parameters	
1	LN	-916	$\mu = -0.44$	$\sigma = 0.15$
	Gamma	-764	$a = 41.45$	$b = 0.02$
2	LN	-851	$\mu = -0.56$	$\sigma = 0.18$
	Gamma	-700	$a = 28.92$	$b = 0.02$
3	LN	-758	$\mu = -0.48$	$\sigma = 0.19$
	Gamma	-643	$a = 28.54$	$b = 0.02$
4	Nakagami	-818	$\alpha = 10.59$	$\xi = 0.50$
	Gamma	-786	$a = 41.22$	$b = 0.02$
5	LN	-681	$\mu = -0.51$	$\sigma = 0.21$
	Gamma	-625	$a = 23.54$	$b = 0.03$
6	LN	-665.1	$\mu = -0.65$	$\sigma = 0.24$
	Gamma	-570	$a = 16.79$	$b = 0.03$
7	LN	-653	$\mu = -0.89$	$\sigma = 0.31$
	Gamma	-460	$a = 9.45$	$b = 0.05$
8	LN	-521	$\mu = -0.76$	$\sigma = 0.31$
	Gamma	-405	$a = 10.2$	$b = 0.05$
9	LN	-741	$\mu = -0.75$	$\sigma = 0.25$
	Gamma	-595	$a = 15.57$	$b = 0.03$
10	LN	-1028	$\mu = -0.43$	$\sigma = 0.14$
	Gamma	-865	$a = 52.82$	$b = 0.01$

- *Sensors on the torso:* We note that shadowing from the right arm experienced by SN8 has the same variation pattern for both CNs. Here, as concerns SN3, it additionally experiences left arm shadowing for the link with CN2.

B. GLOBAL MOBILITY CASE

From the results of Fig. 10, we can notice periodic variations of H_0, which is consistent with the movement patterns of the SNs. Channel gains of the links related to the SNs on the legs and the arms experience more fluctuation than those of SNs on the torso. By observing the dynamics of the SN1 link, which has lower H_0 variations with respect to the local mobility case, we can see that approaching the walls increases the channel gain, which is true for all links. On the other hand, rotations of the body can decrease or increase H_0 significantly depending on whether it is close to or far from a wall.

Comparing the cases of CN1 and CN2, we notice that for SNs located on the arms and the legs, we have a higher H_0 for the case of CN2, whereas, for the SNs located on the upper part of the body, a higher H_0 is obtained with CN1. This is consistent with the observations on the average H_0 made in Section IV.A. For SN2, which is located on the head side, we see similar results for CN1 and CN2.

Lastly, for SN3 and SN5 located on the torso and the arm, we globally observe a local mobility pattern scaled by the global mobility variations.

TABLE 11. Estimated parameters of best fit distributions to H_0 for the case of CN2; global mobility configuration.

SN	Best-fit PDFs	AIC	PDF parameters	
1	LN	-863	$\mu = -0.36$	$\sigma = 0.15$
	Gamma	-812	$a = 45.22$	$b = 0.02$
2	LN	-700	$\mu = -0.69$	$\sigma = 0.24$
	Gamma	-568	$a = 16.5$	$b = 0.03$
3	LN	-567.6	$\mu = -0.85$	$\sigma = 0.33$
	Gamma	-448	$a = 9.32$	$b = 0.05$
4	LN	-634	$\mu = -1.03$	$\sigma = 0.37$
	Gamma	-516	$a = 7.41$	$b = 0.05$
5	LN	-723	$\mu = -1.07$	$\sigma = 0.35$
	Gamma	-590	$a = 8.02$	$b = 0.05$
6	LN	-749	$\mu = -1.09$	$\sigma = 0.35$
	Gamma	-593	$a = 8.06$	$b = 0.05$
7	LN	-918	$\mu = -0.55$	$\sigma = 0.17$
	Gamma	-773	$a = 33.14$	$b = 0.02$
8	LN	-725	$\mu = -1.26$	$\sigma = 0.42$
	Gamma	-568	$a = 5.33$	$b = 0.06$
9	LN	-658	$\mu = -1.04$	$\sigma = 0.36$
	Gamma	-504	$a = 7.35$	$b = 0.05$
10	LN	-426	$\mu = -0.83$	$\sigma = 0.36$
	Gamma	-340	$a = 7.58$	$b = 0.06$

APPENDIX C
BEST-FIT PDFS FOR H_0 FOR INDIVIDUAL SN LINKS

We provide here detailed data on the best-fit PDFs to the H_0 variations for each link between the SNs and the CNs. These are summarized in Tables 10 and 11 for the cases of CN1 and CN2, respectively.

REFERENCES

[1] *Life Expectancy and Healthy Life Expectancy Data by Country*. Accessed: Oct. 04, 2019. [Online]. Available: http://apps.who.int/gho/data/node.main.688?lang=en

[2] C. X. Wong *et al.*, "Epidemiology of sudden cardiac death: Global and regional perspectives," *Heart Lung Circulation*, vol. 28, no. 1, pp. 6–14, Jan. 2019.

[3] *Diabetes*. Accessed: Oct. 4, 2019. [Online]. Available: https://www.who.int/news-room/fact-sheets/detail/diabetes

[4] T. Botsis and G. Hartvigsen, "Current status and future perspectives in telecare for elderly people suffering from chronic diseases," *J. Telemed. Telecare*, vol. 14, no. 4, pp. 195–203, Jan. 2008.

[5] S. Movassaghi, M. Abolhasan, J. Lipman, D. Smith, and A. Jamalipour, "Wireless body area networks: A survey," *IEEE Commun. Surveys Tuts.*, vol. 16, no. 3, pp. 1658–1686, 3rd Quart., 2014.

[6] Z. Ghassemlooy, L. N. Alves, S. Zvànovec, and M. A. Khalighi, Eds., *Visible Light Communications: Theory and Applications*. Boca Raton, FL, USA: CRC Press, 2017.

[7] O. Haddad and M. A. Khalighi, "Enabling communication technologies for medical wireless body-area networks," in *Proc. Global LIFI Congress (GLC)*, Paris, France, Jun. 2019, pp. 1–5.

[8] *IEEE Standard for Local and Metropolitan Area Networks—Part 15.6: Wireless Body Area Networks*, IEEE Standard 802.15.6, Feb. 2012.

[9] D. B. Smith and L. W. Hanlen,*Ultra-Low-Power Short-Range Radios*. Cham, Switzerland: Springer, 2015, ch. Channel Modeling for Wireless Body Area Networks, pp. 25–55.

[10] D. Miniutti *et al.*, *Narrowband Channel Characterization for Body Area Network*, IEEE Standard P802.15-08-0559-00-0006, Jan. 2008.

[11] Z. Ghassemlooy, M. Khalighi, and D. Wu, *Visible Light Communications: Theory and Applications*. Boca Raton, FL, USA: CRC Press, 2017, ch. Channel Modeling, pp. 71–96.

[12] S. Long, M. A. Khalighi, M. Wolf, S. Bourennane, and Z. Ghassemlooy, "Investigating channel frequency selectivity in indoor visible-light communication systems," *IET Optoelectron.*, vol. 10, no. 3, pp. 80–88, Jun. 2016.

[13] J. R. Barry, J. M. Kahn, W. J. Krause, E. A. Lee, and D. G. Messerschmitt, "Simulation of multipath impulse response for indoor wireless optical channels," *IEEE J. Sel. Areas Commun.*, vol. 11, no. 3, pp. 367–379, Apr. 1993.

[14] J. B. Carruthers and P. Kannan, "Iterative site-based modeling for wireless infrared channels," *IEEE Trans. Antennas Propag.*, vol. 50, no. 5, pp. 759–765, May 2002.

[15] Y. A. Alqudah and M. Kavehrad, "MIMO characterization of indoor wireless optical link using a diffuse-transmission configuration," *IEEE Trans. Commun.*, vol. 51, no. 9, pp. 1554–1560, Sep. 2003.

[16] F. J. Lopez-Hernandez, R. Perez-Jimenez, and A. Santamaria, "Ray-tracing algorithms for fast calculation of the channel impulse response on diffuse IR wireless indoor channels," *Opt. Eng.*, vol. 39, no. 10, pp. 2775–2780, 2000.

[17] S. Rodríguez-Perez, R. Pérez-Jiménez, F. J. López-Hernández, O. B. González-Hernández, and A. J. Ayala-Alfonso, "Reflection model for calculation of the impulse response on IR-wireless indoor channels using ray-tracing algorithm," *Microw. Opt. Technol. Lett.*, vol. 32, no. 4, pp. 296–300, 2002.

[18] F. Miramirkhani and M. Uysal, "Channel modeling and characterization for visible light communications," *IEEE Photon. J.*, vol. 7, no. 6, pp. 1–16, Dec. 2015.

[19] H. Schulze, "Frequency-domain simulation of the indoor wireless optical communication channel," *IEEE Trans. Commun.*, vol. 64, no. 6, pp. 2551–2562, Jun. 2016.

[20] J. M. Kahn, W. J. Krause, and J. B. Carruthers, "Experimental characterization of non-directed indoor infrared channels," *IEEE Trans. Commun.*, vol. 43, nos. 2–4, pp. 1613–1623, Feb.–Apr. 1995.

[21] S. M. Mana, P. Hellwig, J. Hilt, P. W. Berenguer, and V. Jungnickel, "Experiments in non-line-of-sight Li-Fi channels," in *Proc. Global LIFI Congr. (GLC)*, Paris, France, Jun. 2019, pp. 1–6.

[22] R. Perez-Jimenez, J. Berges, and M. J. Betancor, "Statistical model for the impulse response on infrared indoor diffuse channels," *Electron. Lett.*, vol. 33, no. 15, pp. 1298–1300, Jul. 1997.

[23] J. B. Carruthers and S. M. Carroll, "Statistical impulse response models for indoor optical wireless channels," *Int. J. Commun. Syst.*, vol. 18, no. 3, pp. 267–284, 2005.

[24] T. Komine, S. Haruyama, and M. Nakagawa, "A study of shadowing on indoor visible-light wireless communication utilizing plural white LED lightings," *Wireless Pers. Commun.*, vol. 34, no. 1, pp. 211–225, Jul. 2005.

[25] Y. Xiang *et al.*, "Human shadowing effect on indoor visible light communications channel characteristics," *Opt. Eng.*, vol. 53, no. 8, pp. 1–8, 2014.

[26] P. Chvojka, S. Zvanovec, P. A. Haigh, and Z. Ghassemlooy, "Channel characteristics of visible light communications within dynamic indoor environment," *J. Lightw. Technol.*, vol. 33, no. 9, pp. 1719–1725, May 01, 2015.

[27] F. Miramirkhani, O. Narmanlioglu, M. Uysal, and E. Panayirci, "A mobile channel model for VLC and application to adaptive system design," *IEEE Commun. Lett.*, vol. 21, no. 5, pp. 1035–1038, May 2017.

[28] M. D. Soltani, A. A. Purwita, Z. Zeng, H. Haas, and M. Safari, "Modeling the random orientation of mobile devices: Measurement, analysis and LiFi use case," *IEEE Trans. Commun.*, vol. 67, no. 3, pp. 2157–2172, Mar. 2019.

[29] A. Julien-Vergonjanne, S. Sahuguède, and L. Chevalier, *Optical Wireless Communications: An Emerging Technology*. Cham, Switzerland: Springer, 2016, ch. Optical Wireless Body Area Networks for Healthcare Applications, pp. 569–587.

[30] A. Behlouli, P. Combeau, and L. Aveneau, "MCMC methods for realistic indoor wireless optical channels simulation," *J. Lightw. Technol.*, vol. 35, no. 9, pp. 1575–1587, May 01, 2017.

[31] H. Behlouli, P. Combeau, S. Sahuguède, A. Julien-Vergonjanne, C. Le Bas, and L. Aveneau, "Impact of physical and geometrical parameters on visible light communication links," in *Proc. Adv. Wireless Opt. Commun. (RTUWO)*, Riga, Latvia, Nov. 2017, pp. 73–76.

[32] C. Le Bas, S. Sahuguede, and A. Julien-Vergonjanne, "Theoretical and experimental approach for the design of an optical wireless physical activity monitoring system," *Int. J. Wireless Inf. Netw.*, vol. 24, no. 2, pp. 65–77, Jun. 2017.

[33] D. R. Dhatchayeny, S. Arya, and Y. H. Chung, "Patient mobility support for indoor non-directed optical body area networks," *Sensors*, vol. 19, no. 10, p. 2297, 2019.

[34] T. B. Hoang, S. Sahuguede, and A. Julien-Vergonjanne, "Optical wireless network design for off-body-sensor based monitoring," *Wireless Commun. Mobile Comput.*, vol. 2019, pp. 1–13, Sep. 2019.

[35] O. Haddad, M. A. Khalighi, and S. Zvanovec, "Channel characterization for optical extra-WBAN links considering local and global user mobility," in *Proc. SPIE 14th Conf. Broadband Access Commun. Technol.*, vol. 11307. San Francisco, CA, USA, Jan. 2020, pp. 89–97.

[36] M. Gallo, P. S. Hall, Y. I. Nechayev, and M. Bozzetti, "Use of animation software in simulation of on-body communications channels at 2.45 GHz," *IEEE Antennas Wireless Propag. Lett.*, vol. 7, pp. 321–324, 2008.

[37] M. Gallo, P. S. Hall, Q. Bai, Y. I. Nechayev, C. C. Constantinou, and M. Bozzetti, "Simulation and measurement of dynamic on-body communication channels," *IEEE Trans. Antennas Propag.*, vol. 59, no. 2, pp. 623–630, Feb. 2011.

[38] T. Uusitupa and T. Aoyagi, "Analysis of dynamic on-body communication channels for various movements and polarization schemes at 2.45 GHz," *IEEE Trans. Antennas Propag.*, vol. 61, no. 12, pp. 6168–6179, Dec. 2013.

[39] S. L. Cotton, W. G. Scanlon, and B. K. Madahar, "Millimeter-wave soldier-to-soldier communications for covert battlefield operations," *IEEE Commun. Mag.*, vol. 47, no. 10, pp. 72–81, Oct. 2009.

[40] M. Mackowiak and L. M. Correia, "A statistical model for the influence of body dynamics on the gain pattern of wearable antennas in off-body radio channels," *Wireless Pers. Commun.*, vol. 73, no. 3, pp. 381–399, May 2013.

[41] K. Turbic, L. M. Correia, and M. Beko, "A mobility model for wearable antennas on dynamic users," *IEEE Access*, vol. 6, pp. 63635–63648, 2018.

[42] H. Ren and M. Q. H. Meng, "Understanding the mobility model of wireless body sensor networks," in *Proc. Int. Conf. Inf. Acquisition*, Weihai, China, Aug. 2006, pp. 306–310.

[43] M. Nabi, M. Geilen, and T. Basten, "MoBAN: A configurable mobility model for wireless body area networks," in *Proc. 4th Int. ICST Conf. Simulat. Tools Techn. (SIMUTools)*, Barcelona, Spain, Mar. 2011, pp. 168–177.

[44] S. N. Pattanaik and S. P. Mudur, "The potential equation and importance in illumination computations," *Comput. Graph. Forum*, vol. 12, no. 2, pp. 131–136, 1993.

[45] P. Dutré, E. Lafortune, and Y. D. Willems, "A mathematical framework for global illumination algorithms," in *Proc. Winter School Comput. Graph. CAD Syst.*, Pilsen, Czech Republic, 1994, pp. 75–84,

[46] C. Bettstetter, H. Hartenstein, and X. Pérez-Costa, "Stochastic properties of the random waypoint mobility model," *Wireless Netw.*, vol. 10, no. 5, pp. 555–567, Sep. 2004.

[47] *Opticstudio*. Accessed: Sep. 16, 2019. [Online]. Available: https://www.zemax.com/products/opticstudio

[48] J. M. Kahn and J. R. Barry, "Wireless infrared communications," *Proc. IEEE*, vol. 85, no. 2, pp. 265–298, Feb. 1997.

[49] A. Fort, C. Desset, P. De Doncker, P. Wambacq, and L. Van Biesen, "An ultra-wideband body area propagation channel model-from statistics to implementation," *IEEE Trans. Microw. Theory Techn.*, vol. 54, no. 4, pp. 1820–1826, Jun. 2006.

[50] *Blender*. Accessed: Sep. 23, 2019. [Online]. Available: https://www.blender.org/

[51] *3D Mesh*. Accessed: May 23, 2020. [Online]. Available: https://3docean.net/item/low-poly-base-mesh-male/73426?WT.ac=category_thumb&WT.seg_1=category_thumb&WT.z_author=karan8/

[52] P. B. Davenport, "Rotations about nonorthogonal axes," *AIAA J.*, vol. 11, no. 6, pp. 853–857, 1973.
[53] F. D. Dinechin and M. Istoan, "Hardware implementations of fixed-point atan2," in *Proc. IEEE 22nd Symp. Comput. Arithmetic*, Lyon, France, Jun. 2015, pp. 34–41.
[54] *Animation Tutorial*. Accessed: May 23, 2020. [Online]. Available: https://www.blendernation.com/2020/05/16/rig-anything-with-rigify-3-prebuilt-meta-rigs-biped-quadruped/
[55] J. E. Graham, S. R. Fisher, I.-M. Bergés, Y.-F. Kuo, and G. V. Ostir, "Walking speed threshold for classifying walking independence in hospitalized older adults," *Phys. Therapy*, vol. 90, no. 11, pp. 1591–1597, Nov. 2010.
[56] R. P. Duncan, M. E. McNeely, and G. M. Earhart, "Maximum step length test performance in people with Parkinson disease: A cross-sectional study," *J. Neurologic Phys. Therapy*, vol. 41, no. 4, pp. 215–221, Oct. 2017.
[57] K. Lee, H. Park, and J. R. Barry, "Indoor channel characteristics for visible light communications," *IEEE Commun. Lett.*, vol. 15, no. 2, pp. 217–219, Feb. 2011.
[58] L. Chevalier, S. Sahuguède, and A. Julien-Vergonjanne, "Optical wireless links as an alternative to radio-frequency for medical body area networks," *IEEE J. Sel. Areas Commun.*, vol. 33, no. 9, pp. 2002–2010, Sep. 2015.
[59] M. Abtahi and H. Hashemi, "Simulation of indoor propagation channel at infrared frequencies in furnished office environments," in *Proc. 6th Int. Symp. Pers. Indoor Mobile Radio Commun.*, vol. 1. Toronto, ON, Canada, Sep. 1995, pp. 306–310.
[60] D. B. Smith, J. Zhang, L. W. Hanlen, D. Miniutti, D. Rodda, and B. Gilbert, "Temporal correlation of dynamic on-body area radio channel," *Electron. Lett.*, vol. 45, no. 24, pp. 1212–1213, Nov. 2009.
[61] M. Mohamed, M. Cheffena, and A. Moldsvor, "Characterization of the body-to-body propagation channel for subjects during sports activities," *Sensors*, vol. 18, no. 2, p. 620, 2018.

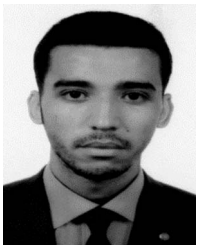

OUSSAMA HADDAD received the B.Sc. and M.Sc. degrees in electrical engineering from the National Polytechnic School of Algiers, Algeria, in 2017. He is currently pursuing the Ph.D. degree with the Fresnel Institute, Ecole Centrale Marseille, France. His research interests include optical wireless communications and wireless body area networks.

MOHAMMAD-ALI KHALIGHI (Senior Member, IEEE) received the Ph.D. degree in telecommunications from the Institut National Polytechnique de Grenoble, Grenoble, France, in 2002. He is currently an Associate Professor with École Centrale Marseille, Marseille, France, and the Head of the Telecommunications and Antenna Processing Group, Fresnel Institute Research Laboratory. He is the Project Coordinator for the H2020 ITN MSCA VisIoN Project (Visible-Light-Based Interoperability and Networking). He has coedited the book *Visible Light Communications: Theory and Applications* (CRC Press, 2017). His main research interests include signal processing for wireless communication systems with an emphasis on the physical layer aspects of free-space, underwater, and indoor visible-light optical communications. He was a co-recipient of the Best Survey Paper Award of the IEEE Communications Society in 2019. He is currently serving as an Editor for the IEEE TRANSACTIONS ON COMMUNICATIONS and has served as an Associate Editor for *IET Electronics Letters* as well as a Guest Co-Editor for the *Optik* (Elsevier).

STANISLAV ZVANOVEC (Senior Member, IEEE) received the M.Sc. and Ph.D. degrees from the Czech Technical University in Prague in 2002 and 2006, respectively, where he is a Full Professor, the Deputy Head of the Department of Electromagnetic Field, and a Leader of Wireless and Fiber Optics Team. He has authored two books and more than 250 journal articles and conference papers. His current research interests include FSO and fiber optical systems, VLC, and RF over optics.

MOULOUD ADEL has been a Professor of computer science and electrical engineering with Aix-Marseille University, Marseille, France, since 2014. He has been involved in many international research programs His research areas concern signal and image processing and machine learning applied to biomedical and industrial images. He is a member of the editorial board of *Journal of Biomedical Engineering and Informatics*. He has been an invited speaker at different universities and has been the co-organizer of various international conferences and workshops.